



Article

Threefold Fermions, Weyl Points, and Superconductivity in the Mirror Symmetry Lacking Semiconductor TlCd_2Te_4

Angus Huang^{1,2,†}, Chin-Hsuan Chen^{1,†} and Horng-Tay Jeng^{1,3,4,*}

¹ Department of Physics, National Tsing Hua University, Hsinchu 30013, Taiwan; rabbit4a9@gmail.com (A.H.); barry810929@gmail.com (C.-H.C.)

² Department of Physics, National Cheng Kung University, Tainan 70101, Taiwan

³ Physics Division, National Center for Theoretical Sciences, Hsinchu 30013, Taiwan

⁴ Institute of Physics, Academia Sinica, Taipei 11529, Taiwan

* Correspondence: jeng@phys.nthu.edu.tw

† These authors contributed equally to this work.

Abstract: The topological phase transition and exotic quasiparticles in materials have attracted much attention because of their potential in spintronics and mimic of elementary particles. Especially, great research interest has been paid to search for the Weyl fermions in solid-state physics. By using first-principles calculations, we predict that the multinary semiconductor alloy TlCd_2Te_4 exhibits threefold fermions and nodal-line fermions, which are protected by the S_4 improper rotational symmetry. Moreover, owing to the lack of inversion and mirror symmetries, the threefold fermions split into Weyl fermions when the spin-orbit coupling is included. The chiral charge of Weyl points and the Z_2 time-reversal topological invariant are investigated. The topological surface states, spin texture, and electron-phonon coupling analysis are presented. Our study demonstrates TlCd_2Te_4 as a good platform to understand topological phase transitions as well as possible coexistence of topological Weyl semimetal and superconductivity in one single material.



Citation: Huang, A.; Chen, C.-H.; Jeng, H.-T. Threefold Fermions, Weyl Points, and Superconductivity in the Mirror Symmetry Lacking Semiconductor TlCd_2Te_4 .

Nanomaterials **2022**, *12*, 679. <https://doi.org/10.3390/nano12040679>

Academic Editor: Sławomir P. Lepkowski

Received: 29 December 2021

Accepted: 15 February 2022

Published: 18 February 2022

Publisher's Note: MDPI stays neutral with regard to jurisdictional claims in published maps and institutional affiliations.



Copyright: © 2022 by the authors. Licensee MDPI, Basel, Switzerland. This article is an open access article distributed under the terms and conditions of the Creative Commons Attribution (CC BY) license (<https://creativecommons.org/licenses/by/4.0/>).

Keywords: threefold fermions; Weyl points; superconductivity

1. Introduction

Since the research of topological materials, the quasiparticles in solid-state materials have provided a tabletop platform to imitate the particles in high-energy physics. Several kinds of particles have been discovered by experiments or theoretical predictions, such as the Dirac fermions [1–3], Weyl fermions [4,5], and spin-3/2 Rarita-Schwinger-Weyl (RSW) fermions [6]. Furthermore, some quasiparticles beyond particle physics have also been demonstrated in materials, for example, type-II Dirac/Weyl fermions [7,8], nodal-line [9,10], quadratic or cubic Weyl fermions [11,12], hourglass fermions [13–15], and high-fold fermions [6,16–21]. The topological phase transitions also give a route to study the interaction between elementary particles.

In particular, Weyl fermions have attracted much interest because of the predictions but non-observed in elementary particle physics. It has been theoretically predicted [8] and experimentally observed [22] that Dirac fermions could split into Weyl fermions. However, the phase transitions of Weyl fermions to other exotic fermions, such as the threefold fermions (TFFs, also known as three-component fermions [18], triple-point fermions [21]), have not been discovered yet.

In this work, using first-principles calculations based on density functional theory (DFT), we study the multinary semiconductor alloy material TlCd_2Te_4 , which has been synthesized by previous experiments [23]. Two TFFs and nodal-line fermions in TlCd_2Te_4 stemmed from the S_4 improper rotational symmetry are demonstrated. When spin-orbit coupling is included, owing to the lack of inversion and mirror symmetries, a topological phase transition occurs and each TFFs split into four Weyl points (WPs) with chiral charge

$C = \pm 1$. The Z_2 topological invariant $v_{Z_2} = 1$ are also proved by Wilson loops (WLs) analysis. We also present the topological surface states (TSSs) of TlCd_2Te_4 , which may be observed in future experiments. Finally, we also show the stable phonon bands of TlCd_2Te_4 as well as the superconductivity of $T_C = 3.8$ K after electron doping of 0.5 e/f.u.

2. Method

The first-principles calculations are carried out using Vienna Ab-initio Simulation Package (VASP) [24,25] utilizing the Ceperly-Alder (CA) type exchange-correlation functional and all-electron projected augmented wave (PAW) method within the framework of local density approximation (LDA) [26] based on density functional theory (DFT). The $12 \times 12 \times 12$ k -grids over the first Brillouin zone (BZ) with the energy cut-off of 400 eV are used in the self-consistent calculations. The lattice structure and space group of TlCd_2Te_4 is obtained from previous experiments [23]. Then, the lattice parameters and positions of ions are optimized until the residual atomic forces are less than 0.03 eV/Å. The tight-binding Hamiltonian with Wannier basis is constructed from Te- p orbitals using the *vasp2wannier90* interface [27]. For topological properties, such as the Wilson loop (WL) [28,29], Z_2 topological invariant, and chiral charge, simulations are performed using the formula [30]

$$\phi_m = -\text{im} \log \sum_i \langle \mathbf{k}_i | \mathbf{k}_{i+1} \rangle. \quad (1)$$

Here ϕ_m and $|\mathbf{k}_i\rangle$ are the Berry phase and the wave functions of the m th band and i th k -point, respectively. The semi-infinite Green functions of surface states are simulated using the Sancho-Rubio method [31]. The quasiparticle interference (QPI) $\chi(\mathbf{q}, E)$ are computed through the spin-dependent joint density of states (JDOS) [32,33]

$$\chi(\mathbf{q}, E) = \sum_{\mathbf{k}, i} \mathcal{A}^i(\mathbf{k}, E) \mathcal{A}^i(\mathbf{k} + \mathbf{q}, E) \quad (2)$$

with

$$\mathcal{A}^i(\mathbf{k}, E) \equiv \langle S_i(\mathbf{k}, E) \rangle = -\text{im} \text{tr}(G(\mathbf{k}, E) \sigma^i). \quad (3)$$

Here \mathcal{A}^i , S_i , and G are the spin-dependent spectrum, spin operator, and Green functions of surface states, respectively. σ^i ($i = 0, 1, 2, 3$) are the identity matrix ($i = 0$) and Pauli matrix ($i = 1, 2, 3$). The 400×400 k -mesh are used in QPI simulations.

For phonon and electron-phonon coupling simulations, the density functional perturbation theory (DFPT) calculations are performed using the quantum espresso package [34] over the k -mesh (q -mesh) of $32 \times 32 \times 32$ ($4 \times 4 \times 4$). Superconducting T_C is estimated by the Allen-Dynes modified McMillan formula [35]

$$T_C = f_1 f_2 \frac{\bar{\omega}_{\log}}{1.2} \exp\left(\frac{1.04(1 + \lambda)}{\mu^*(1 + 0.62\lambda) - \lambda}\right) \quad (4)$$

and Eliashberg function $\alpha^2 F(\omega)$

$$\alpha^2 F(\omega) = \frac{1}{2} \int_{\text{BZ}} \lambda_{qv} \omega_{qv} \delta(\omega - \omega_{qv}) dq. \quad (5)$$

Here ω_{qv} ($\bar{\omega}_{\log}$) is the phonon band (logarithmic average phonon) frequency. The λ (λ_{qv}) is the electron-phonon coupling strength (electron-phonon coupling coefficient of each band), from the DFPT calculations. Furthermore, we calculate the integral of λ_{qv} , $\lambda(\omega) \equiv \int^{\omega} \sum_{qv} \lambda_{qv} dq$. The μ^* is the effective Coulomb repulsion, we choose $\mu^* = 0.1$ in this work as is commonly used in superconductivity calculations. f_1 and f_2 are the same as those given by Allen and Dynes [35].

3. Electronic Structures

The multinary semiconductor alloy TlCd_2Te_4 has been synthesized by previous experiments [23]. Based on experimental results, TlCd_2Te_4 has space group $I\bar{4}$ (#82) with thiogallate structure (defect-chalcopyrite structure, also presented in ordered-vacancy compounds of AB_2X_4 [36]), which lacks the inversion symmetry while keeps an S_4 improper rotational symmetry in the z -direction. Unlike the well-known Weyl semimetals such as TaAs and $1T^d - \text{WTe}_2$, TlCd_2Te_4 , however, has no mirror symmetry, which makes it a special case in the Weyl family. The lattice structure and atomic positions of TlCd_2Te_4 have been geometrically relaxed in our DFT calculations. The optimized lattice constants are $a = 6.16 \text{ \AA}$ and $c = 12.57 \text{ \AA}$. Each Tl/Cd ion is surrounded by four Te ions, forming $\text{TlTe}_4/\text{CdTe}_4$ tetrahedrons, as shown in Figure 1a. All $\text{TlTe}_4/\text{CdTe}_4$ tetrahedrons rotate a small angle along the z -axis as presented in Figure 1b, which breaks the inversion symmetry and mirror symmetry of TlCd_2Te_4 .

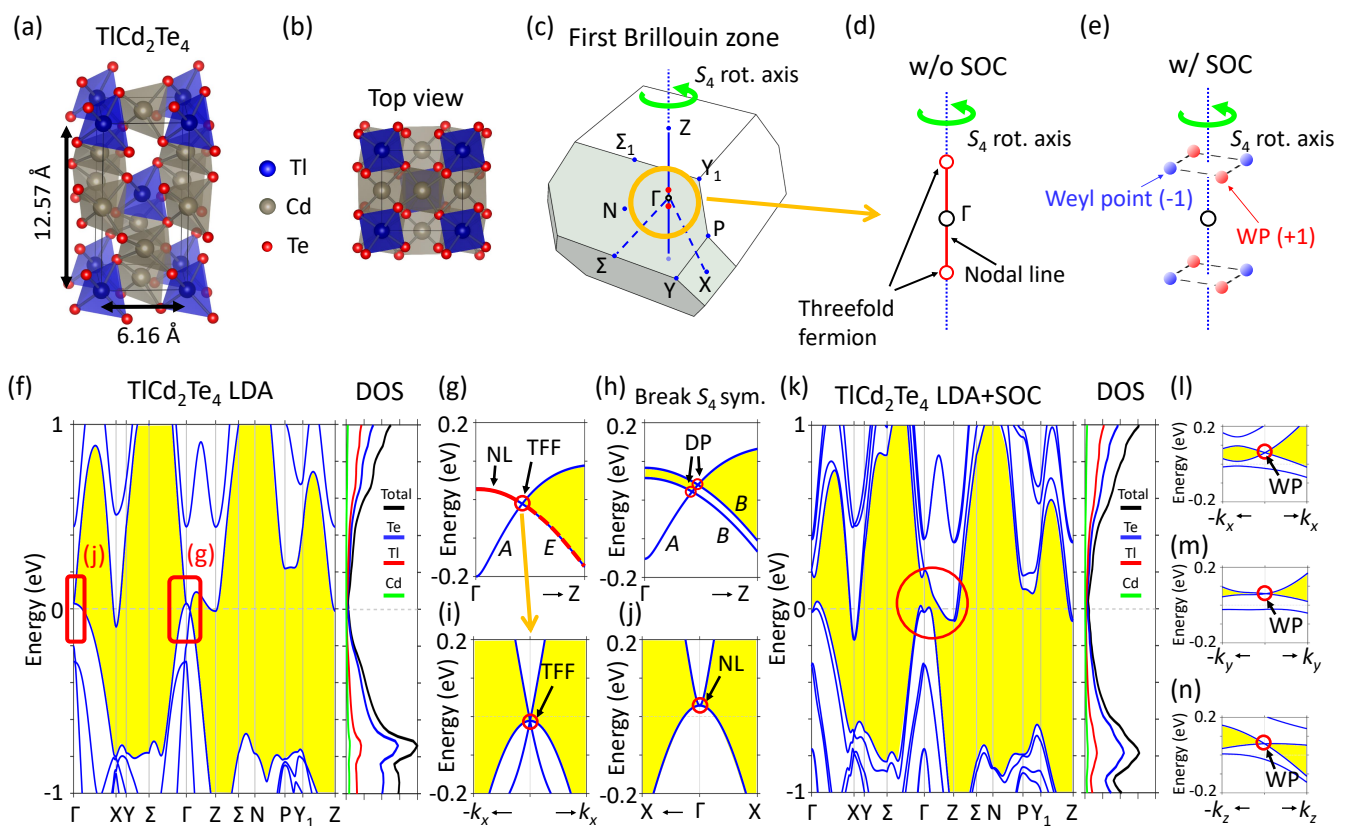


Figure 1. The lattice and band structure of TlCd_2Te_4 . (a) The lattice structure and parameters of TlCd_2Te_4 . (b) The top view of TlCd_2Te_4 . (c) The first Brillouin zone of TlCd_2Te_4 . The red points indicate the threefold fermion. (d) The sketch of threefold fermions and nodal-line in the Brillouin zone. (e) The 2 threefold fermions in (d) split into 8 Weyl points due to SOC. (f) The band structure and DOS of TlCd_2Te_4 . (g) The zoom-in of threefold fermion (TFF). (h) The band structures with breaking S_4 symmetry. (i) The TFF in the k_x direction. (j) the nodal-line at Γ point in the XTX direction. (k) The band structure and DOS with SOC. (l–n) The band structure of Weyl point (WP) along different directions.

The band structure of TlCd_2Te_4 along high-symmetry lines in Brillouin zone (BZ) (Figure 1c) calculated using LDA is shown in Figure 1f. The bands near the Fermi level are dominated by Te- p orbitals. There exists a continuous energy band gap as highlighted by the yellow region with only two band crossing points around the Γ -point as indicated by the red rectangles. The zoom-in pictures of these band crossings are presented in Figure 1g,j. The band crossing (red circle in Figure 1g) between the Γ and Z is composed of a single

band (blue line) with a double degenerate nodal-line band (red-on-blue line in Figure 1g). To verify if this crossing is protected by S_4 symmetry, we studied the character of this eigenstate from the tight-binding model with Wannier orbitals. The symmetry analysis demonstrates that the nodal-line and single band have eigenvalues of $\pm i$ and $+1$ in S_4 symmetry denoted by E and A , respectively, in the group representations [37], as shown in Figure 1g. Their different group representations assure that this band crossing is S_4 symmetry protected TFF. Moreover, owing to the S_4 symmetry, the TFF come in pairs: one along $+k_z$ and the other along $-k_z$, with the nodal-line connecting them as sketched in Figure 1d. The S_4 protected nodal-line also presents another band crossing in $X\Gamma X$, as shown in Figure 1j. Owing to the lack of S_4 symmetry away from ΓZ axis, the double degenerate nodal-line at TFF in the ΓZ axis splits into two bands along the k_x -direction as presented in Figure 1i. On the other hand, we break the S_4 symmetry by artificially moving some ions while keeping the C_2 symmetry. Without the S_4 symmetry, the nodal-line splits into two bands with eigenvalues of -1 in the C_2 symmetry. The TFF thus splits into two Dirac points as demonstrated in Figure 1h. This result, combined with previous group representation analysis, clearly proves that both TFFs and nodal-line are protected by S_4 symmetry.

To study the topological properties, the spin-orbit coupling (SOC) is included in the calculations of band structures as illustrated in Figure 1k. As can be seen, SOC removes all the band crossings from the high-symmetry lines, as highlighted by the red circle in Figure 1k. In comparison with Figure 1f, SOC also opens up an energy gap of ~ 0.2 eV around the Γ -point, which serves as a rough estimation of the strength of SOC in TlCd_2Te_4 . However, the lack of inversion symmetry implies that Weyl points (WPs) could exist in non-high symmetry k -points. We use the tight-binding model with Wannier orbitals to find the band crossings in the full first Brillouin zone. Eight WPs in total are found as shown in Figure 1e. One of the WPs locates at $\mathbf{k}_{\text{WP1}} = (0.042, 0.012, 0.120) \text{ \AA}^{-1}$, and the other seven WPs are symmetric to the first one. The evolution from TFF to WPs due to SOC can be seen in comparison with Figure 1d,e: SOC splits each TFF into four WPs. DFT band structures of one selected WP are shown in Figure 1l–n, which present strong anisotropy in band structures. Furthermore, the linear band dispersions imply the WPs carry the chiral charge $C = \pm 1$.

4. Topological Phases, Surface State, and QPI

The Berry phase and Wilson loop (WL) of TlCd_2Te_4 shown in Figure 2 are calculated on the sphere surrounding the crossing points illustrated in Figure 2d. Previous studies of TFF with SOC present the topological properties with Chern number $C = 2$ [38]. For TlCd_2Te_4 , the WLs of TFFs present zero times winding without SOC, that is $C = 0$ as shown in Figure 2a. Nevertheless, the Berry phase present a sharp change in $k_\theta \simeq 0.3\pi$ and $k_\theta \simeq 0.7\pi$ with the opposite-sign, which implies the non-zero Berry curvature on the sphere and topological invariants could be induced when the SOC is included. For the Weyl semimetals with mirror symmetry, such as TaAs and $1T^d - \text{WTe}_2$, the WPs are produced in pairs by SOC on both sides of the mirror symmetry planes. However, owing to the lack of mirror symmetry, one TFF splits into four WPs with different chiral charges in TlCd_2Te_4 . The chiral charge ($C = \pm 1$) of different WPs, from the WL results, are shown in Figure 2b,c. To confirm the topological properties of TlCd_2Te_4 , the Z_2 topological invariant is provided in Figure 2e,f. The WLs show different winding numbers of 1 and 0 in different plane $k_c = 0$ and $k_c = 0.5$. This WLs result shows that TlCd_2Te_4 also exhibits the non-trivial strong topological insulator property $\nu_{Z_2} = 1$. From our knowledge, this topological phase transition from TFF to Weyl semimetal induced by SOC has not been reported to date.

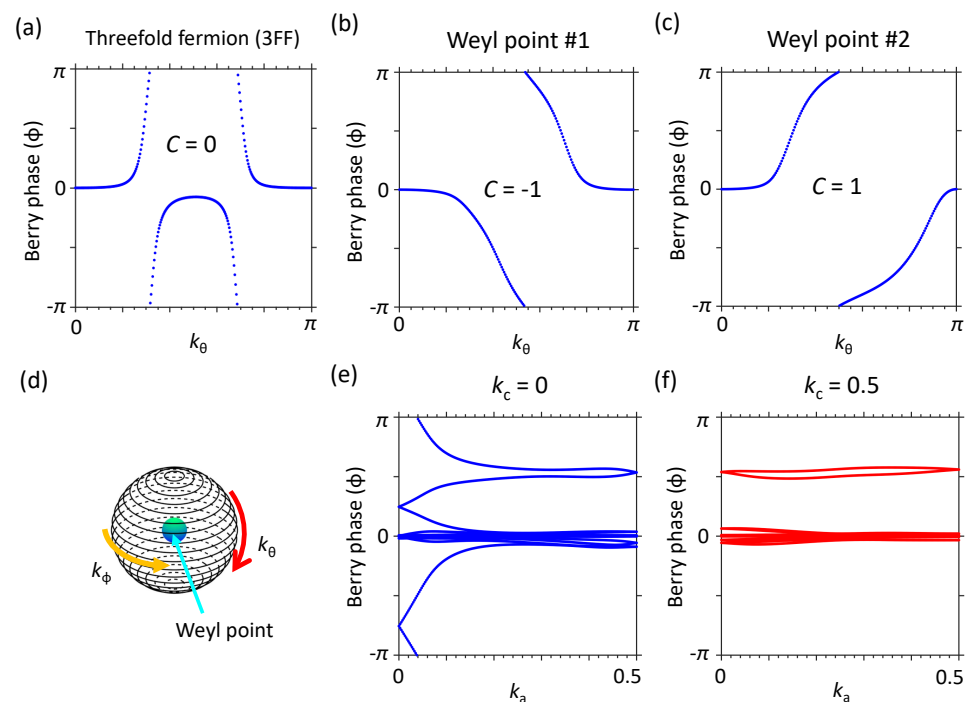


Figure 2. (a) The Wilson loop (WL) of TFF of TlCd_2Te_4 . (b,c) The WL at two different WPs (WPs). (d) The sphere surrounding the crossing point for simulating the WL. (e,f) The WL of Z_2 topological invariant.

The WPs with different chiral charges presented in Figure 3a are close to each other and covered by bulk bands, which makes the WPs barely visible. The topological surface states (TSS) calculated using the semi-infinite slab Green function simulations for (100) surface are presented in Figure 3b. As highlighted by the short green arrow, the TSSs connect the valence bands with the conduction bands, demonstrating the Z_2 topological invariant behavior. Figure 3c shows the two-dimensional contour of TSSs at the same energy as that of the Weyl points ($E = 0.06$ eV). The TSSs connect the WPs and then extend into the bulk bands as surface resonance states (SRSs). Two parallelogram-shaped Fermi arcs (TSSs) connecting two WPs with different chiral charge can be seen. We have also performed the QPI simulations as shown in Figure 3d. The correlations (green arrows in Figure 3c) between parallelogram-shaped topological surface states forms a cross-shaped QPI, which is different from the common circle-shaped QPI. The spin textures of TSSs $\langle S_i \rangle = \mathcal{A}^i(\mathbf{k}, E)$ obtained from Equation (3) are shown in Figure 3e. Owing to the SOC, the spin of SSs rotate around the $\tilde{\Gamma}$. Moreover, we also show the spin textures of the SRSs at $E = 0.52$ eV in Figure 3f, which corresponds to the electron doping of $0.5 e$ per formula unit ($0.5 e/f.u.$).

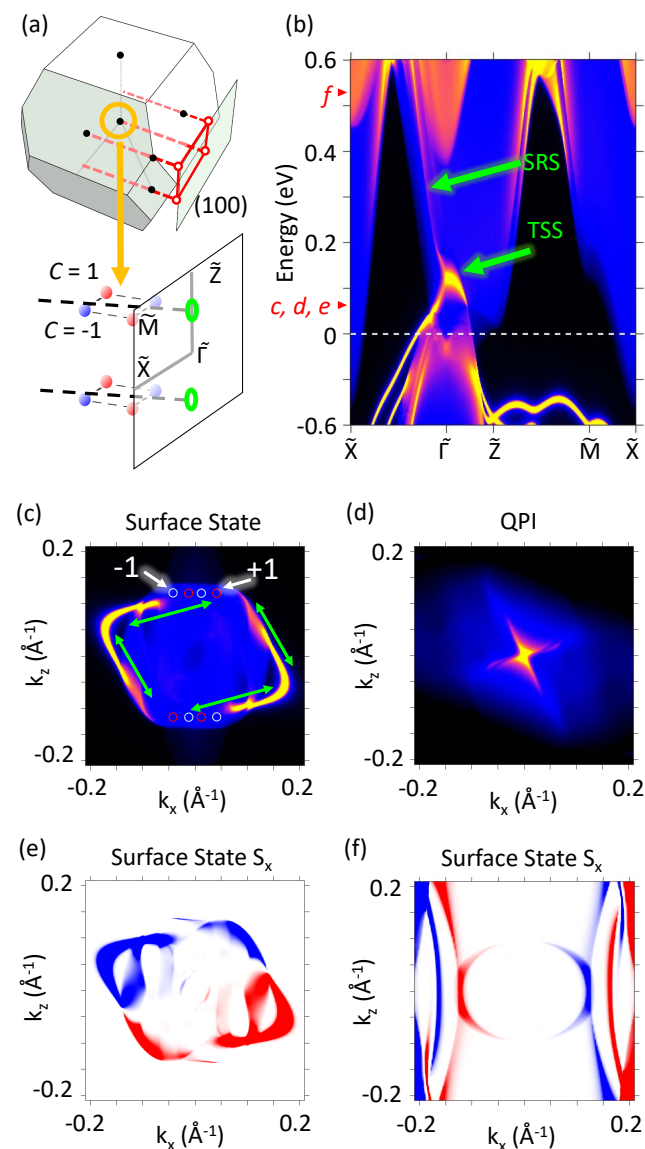


Figure 3. (a) The Brillouin zone and WPs projected onto the (100) surface. (b) The surface states calculated from semi-infinite Green function method. The small red arrows on the energy axis show the energies of subfigures (c–f). (c) The two-dimensional contour of BZ at $E = 0.06$ eV on (100). The red (light blue) circles indicate the projection of Weyl point with chiral charge +1 (−1). (d) Cross-shaped QPI. (e) $\langle S_x \rangle$ of TSSs at $E = 0.06$ eV. (f) $\langle S_x \rangle$ of SRSs at $E = 0.52$ eV.

5. Phonon Band and Superconductivity

The phonon band structure and electron-phonon coupling strength λ of pristine TlCd_2Te_4 and $0.5 e/f.u.$ electron doped TlCd_2Te_4 are studied by using DFPT calculations. The phonon bands, $\lambda(\omega)$, and Eliashberg function are shown in Figure 4a,b. All the phonon bands are well behaved without imaginary phonon modes, showing that the structure of TlCd_2Te_4 is stable. The electron-phonon coupling strength $\lambda = 0.18$ presents the non-superconductivity in pristine TlCd_2Te_4 . However, after doping electrons of $0.5 e/f.u.$ as shown in Figure 4c, Kohn-anomalies highlighted by blue arrows are thus induced at X and Z points with strong electron-phonon coupling strength. It can be seen that the strongly enhanced electron-phonon coupling is significantly correlated with the softened phonon modes with relatively lower phonon energies forming the Kohn-anomalies. This is presumably due to the raised Fermi level up to 0.52 eV which may results in possible Fermi nesting among the Fermi pockets originated from the multi-valleys around 0.5 eV

(Figure 1f,k). Moreover, the superconductivity emerges with $T_C = 3.8$ K due to the highly raised $\lambda = 0.94$. The result shows that suitable electron doping in TlCd_2Te_4 could lead to a good platform for studying the superconductivity and topological Weyl semimetal coexisted system.

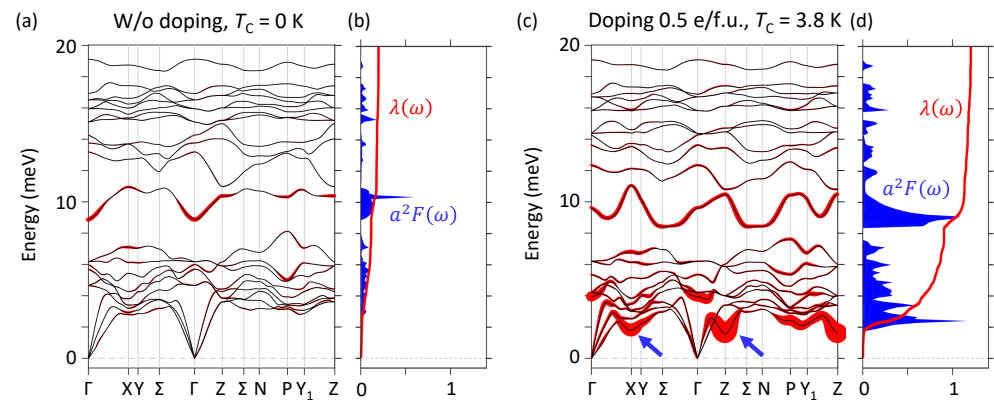


Figure 4. (a) The phonon band structure and electron-phonon coupling strength (red circle) of pristine TlCd_2Te_4 . (b) The electron-phonon coupling strength λ and Eliashberg function α^2F of pristine TlCd_2Te_4 . (c) The phonon band structure and electron-phonon coupling strength of 0.5 e/f.u. electron doped TlCd_2Te_4 . (d) The corresponding λ and α^2F of 0.5 e/f.u. electron doped TlCd_2Te_4 .

6. Discussion and Conclusions

Previous DFT works have demonstrated the mirror symmetry lacking Weyl semimetal SrSi_2 [11]. Also, the topological phase transitions from TFFs to WPs have been predicted in BaAgAs by artificial breaking the inversion symmetry [39]. However, the topological phase transitions from TFFs to WPs induced by SOC demonstrated in our work have not been reported to date. Thus TlCd_2Te_4 serves as a prototype material for studying the evolution of high-fold fermions beyond previous researches.

We note that because the defect is conceded as changing the electron numbers in the calculations, it has small influence to TlCd_2Te_4 only. For real cases, doping might break more symmetry in TlCd_2Te_4 . However, owing that these Weyl points are not protected by the crystal symmetries, the topological properties of TlCd_2Te_4 will not be changed by doping.

The robustness of topological properties and phase transaction are also important issues. We have further examined the strain effect on the topological properties of TlCd_2Te_4 by applying uniform strain of -2% and -5% , which correspond to pressure of 2 GPa and 5.5 GPa, respectively. In both cases, the TFF and Weyl fermions move slightly in k-space with the topological properties kept unchanged. Thus the topological properties of TlCd_2Te_4 are robust against strain effect.

In conclusion, using first-principle simulations, we study the topological properties and invariants in TlCd_2Te_4 in this work. We show that the lacking of inversion and mirror symmetries in TlCd_2Te_4 leads to the exotic topological phase. The splitting of threefold fermions (TFFs) into Weyl points (WPs) induced by SOC are demonstrated. The topological invariants, such as chiral charge and Z_2 , and Fermi arc states have been studied in detail. Moreover, the phonon band structures and superconductivity with $T_C = 3.8$ K for electron doped TlCd_2Te_4 are also obtained by using DFPT. Our study sheds lights to a new evolution of topological phase transitions, as well as the possible coexistence of superconductivity and topological Weyl semimetal in one single material.

Author Contributions: Investigation, A.H. and C.-H.C.; Resources, H.-T.J.; Supervision, H.-T.J.; Writing—original draft, A.H.; Writing—review & editing, A.H. and H.-T.J. All authors have read and agreed to the published version of the manuscript.

Funding: This research received no external funding.

Institutional Review Board Statement: Not applicable.

Informed Consent Statement: Not applicable.

Data Availability Statement: Not applicable.

Acknowledgments: This work was supported by the Ministry of Science and Technology, Taiwan. H.-T.J. also thanks support from NCHC, CINC-NTU, AS-iMATE-109-13, and CQT-NTHU-MOE, Taiwan.

Conflicts of Interest: The authors declare no conflict of interest.

References

1. Liu, Z.K.; Zhou, B.; Zhang, Y.; Wang, Z.J.; Weng, H.M.; Prabhakaran, D.; Mo, S.K.; Shen, Z.X.; Fang, Z.; Dai, X.; et al. Discovery of a Three-Dimensional Topological Dirac Semimetal, Na_3Bi . *Science* **2014**, *343*, 864–867. [[CrossRef](#)] [[PubMed](#)]
2. Wang, Z.; Sun, Y.; Chen, X.Q.; Franchini, C.; Xu, G.; Weng, H.; Dai, X.; Fang, Z. Dirac semimetal and topological phase transitions in A_3Bi ($\text{A} = \text{Na}, \text{K}, \text{Rb}$). *Phys. Rev. B* **2012**, *85*, 195320. [[CrossRef](#)]
3. Wang, Z.; Weng, H.; Wu, Q.; Dai, X.; Fang, Z. Three-dimensional Dirac semimetal and quantum transport in Cd_3As_2 . *Phys. Rev. B* **2013**, *88*, 125427. [[CrossRef](#)]
4. Lv, B.Q.; Xu, N.; Weng, H.M.; Ma, J.Z.; Richard, P.; Huang, X.C.; Zhao, L.X.; Chen, G.F.; Matt, C.E.; Bisti, F.; et al. Observation of Weyl nodes in TaAs. *Nat. Phys.* **2015**, *11*, 724–727. [[CrossRef](#)]
5. Huang, S.M.; Xu, S.Y.; Belopolski, I.; Lee, C.C.; Chang, G.; Wang, B.; Alidoust, N.; Bian, G.; Neupane, M.; Zhang, C.; et al. A Weyl Fermion semimetal with surface Fermi arcs in the transition metal monpnictide TaAs class. *Nat. Commun.* **2015**, *6*, 7373. [[CrossRef](#)] [[PubMed](#)]
6. Tang, P.; Zhou, Q.; Zhang, S.C. Multiple Types of Topological Fermions in Transition Metal Silicides. *Phys. Rev. Lett.* **2017**, *119*, 206402. [[CrossRef](#)]
7. Soluyanov, A.A.; Gresch, D.; Wang, Z.; Wu, Q.; Troyer, M.; Dai, X.; Bernevig, B.A. Type-II Weyl semimetals. *Nature* **2015**, *527*, 495–498. [[CrossRef](#)]
8. Chang, T.R.; Xu, S.Y.; Sanchez, D.S.; Tsai, W.F.; Huang, S.M.; Chang, G.; Hsu, C.H.; Bian, G.; Belopolski, I.; Yu, Z.M.; et al. Type-II Symmetry-Protected Topological Dirac Semimetals. *Phys. Rev. Lett.* **2017**, *119*, 026404. [[CrossRef](#)]
9. Bian, G.; Chang, T.R.; Sankar, R.; Xu, S.Y.; Zheng, H.; Neupert, T.; Chiu, C.K.; Huang, S.M.; Chang, G.; Belopolski, I.; et al. Topological nodal-line fermions in spin-orbit metal PbTaSe_2 . *Nat. Commun.* **2016**, *7*, 10556. [[CrossRef](#)]
10. Fu, B.B.; Yi, C.J.; Zhang, T.T.; Caputo, M.; Ma, J.Z.; Gao, X.; Lv, B.Q.; Kong, L.Y.; Huang, Y.B.; Richard, P.; et al. Dirac nodal surfaces and nodal lines in ZrSiS . *Sci. Adv.* **2019**, *5*, eaau6459. [[CrossRef](#)]
11. Huang, S.M.; Xu, S.Y.; Belopolski, I.; Lee, C.C.; Chang, G.; Chang, T.R.; Wang, B.; Alidoust, N.; Bian, G.; Neupane, M.; et al. New type of Weyl semimetal with quadratic double Weyl fermions. *Proc. Natl. Acad. Sci. USA* **2016**, *113*, 1180–1185. [[CrossRef](#)] [[PubMed](#)]
12. Fang, C.; Gilbert, M.J.; Dai, X.; Bernevig, B.A. Multi-Weyl Topological Semimetals Stabilized by Point Group Symmetry. *Phys. Rev. Lett.* **2012**, *108*, 266802. [[CrossRef](#)]
13. Alexandradinata, A.; Wang, Z.; Bernevig, B.A. Topological Insulators from Group Cohomology. *Phys. Rev. X* **2016**, *6*, 021008. [[CrossRef](#)]
14. Kuo, C.S.; Chang, T.R.; Xu, S.Y.; Jeng, H.T. Unconventional topological phase transition in non-symmorphic material KHgX ($\text{X} = \text{As}, \text{Sb}, \text{Bi}$). *npj Comput. Mater.* **2019**, *5*, 1–7. [[CrossRef](#)]
15. Wang, Z.; Alexandradinata, A.; Cava, R.J.; Bernevig, B.A. Hourglass fermions. *Nature* **2016**, *532*, 189–194. [[CrossRef](#)] [[PubMed](#)]
16. Bradlyn, B.; Cano, J.; Wang, Z.; Vergniory, M.G.; Felser, C.; Cava, R.J.; Bernevig, B.A. Beyond Dirac and Weyl fermions: Unconventional quasiparticles in conventional crystals. *Science* **2016**, *353*, aaf5037. [[CrossRef](#)] [[PubMed](#)]
17. Ma, J.Z.; He, J.B.; Xu, Y.F.; Lv, B.Q.; Chen, D.; Zhu, W.L.; Zhang, S.; Kong, L.Y.; Gao, X.; Rong, L.Y.; et al. Three-component fermions with surface Fermi arcs in tungsten carbide. *Nat. Phys.* **2018**, *14*, 349–354. [[CrossRef](#)]
18. Lv, B.Q.; Feng, Z.L.; Xu, Q.N.; Gao, X.; Ma, J.Z.; Kong, L.Y.; Richard, P.; Huang, Y.B.; Strocov, V.N.; Fang, C.; et al. Observation of three-component fermions in the topological semimetal molybdenum phosphide. *Nature* **2017**, *546*, 627–631. [[CrossRef](#)]
19. Krempaský, J.; Nicolaï, L.; Gmitra, M.; Chen, H.; Fanciulli, M.; Guedes, E.B.; Caputo, M.; Radović, M.; Volobuev, V.V.; Caha, O.; et al. Triple-Point Fermions in Ferroelectric GeTe . *Phys. Rev. Lett.* **2021**, *126*, 206403. [[CrossRef](#)]
20. Hasan, M.Z.; Chang, G.; Belopolski, I.; Bian, G.; Xu, S.Y.; Yin, J.X. Weyl, Dirac and high-fold chiral fermions in topological quantum matter. *Nat. Rev. Mater.* **2021**, *6*, 784–803. [[CrossRef](#)]
21. Zhu, Z.; Winkler, G.W.; Wu, Q.; Li, J.; Soluyanov, A.A. Triple Point Topological Metals. *Phys. Rev. X* **2016**, *6*, 031003. [[CrossRef](#)]
22. Li, C.Z.; Wang, L.X.; Liu, H.; Wang, J.; Liao, Z.M.; Yu, D.P. Giant negative magnetoresistance induced by the chiral anomaly in individual Cd_3As_2 nanowires. *Nat. Commun.* **2015**, *6*, 10137. [[CrossRef](#)] [[PubMed](#)]
23. Tomashyk, V.; Feychuk, P.; Shcherbak, L. *Multinary Alloys Based on III–V Semiconductors*; Taylor & Francis: Boca Raton, FL, USA, 2021.
24. Kresse, G.; Furthmüller, J. Efficiency of ab-initio total energy calculations for metals and semiconductors using a plane-wave basis set. *Comput. Mater. Sci.* **1996**, *6*, 15–50. [[CrossRef](#)]

25. Kresse, G.; Furthmüller, J. Efficient iterative schemes for ab initio total-energy calculations using a plane-wave basis set. *Phys. Rev. B* **1996**, *54*, 11169–11186. [[CrossRef](#)] [[PubMed](#)]
26. Ceperley, D.M.; Alder, B.J. Ground State of the Electron Gas by a Stochastic Method. *Phys. Rev. Lett.* **1980**, *45*, 566–569. [[CrossRef](#)]
27. Franchini, C.; Kováčik, R.; Marsman, M.; Murthy, S.S.; He, J.; Ederer, C.; Kresse, G. Maximally localized Wannier functions in LaMnO₃ within PBE + U, hybrid functionals and partially self-consistent GW: An efficient route to construct ab initio tight-binding parameters for eg perovskites. *J. Phys. Condens. Matter* **2012**, *24*, 235602. [[CrossRef](#)]
28. Soluyanov, A.A.; Vanderbilt, D. Wannier representation of \mathbb{Z}_2 topological insulators. *Phys. Rev. B* **2011**, *83*, 035108. [[CrossRef](#)]
29. Yu, R.; Qi, X.L.; Bernevig, A.; Fang, Z.; Dai, X. Equivalent expression of \mathbb{Z}_2 topological invariant for band insulators using the non-Abelian Berry connection. *Phys. Rev. B* **2011**, *84*, 075119. [[CrossRef](#)]
30. Vanderbilt, D. *Berry Phases in Electronic Structure Theory: Electric Polarization, Orbital Magnetization and Topological Insulators*; Cambridge University Press: Cambridge, UK, 2018. [[CrossRef](#)]
31. Sancho, M.P.L.; Sancho, J.M.L.; Sancho, J.M.L.; Rubio, J. Highly convergent schemes for the calculation of bulk and surface Green functions. *J. Phys. F Met. Phys.* **1985**, *15*, 851–858. [[CrossRef](#)]
32. Kohsaka, Y.; Machida, T.; Iwaya, K.; Kanou, M.; Hanaguri, T.; Sasagawa, T. Spin-orbit scattering visualized in quasiparticle interference. *Phys. Rev. B* **2017**, *95*, 115307. [[CrossRef](#)]
33. Guan, S.Y.; Chen, P.J.; Chu, M.W.; Sankar, R.; Chou, F.; Jeng, H.T.; Chang, C.S.; Chuang, T.M. Superconducting topological surface states in the noncentrosymmetric bulk superconductor PbTaSe₂. *Sci. Adv.* **2016**, *2*, e1600894. [[CrossRef](#)] [[PubMed](#)]
34. Giannozzi, P.; Andreussi, O.; Brumme, T.; Bunau, O.; Nardelli, M.B.; Calandra, M.; Car, R.; Cavazzoni, C.; Ceresoli, D.; Cococcioni, M.; et al. Advanced capabilities for materials modelling with Quantum ESPRESSO. *J. Phys. Condens. Matter.* **2017**, *29*, 465901. [[CrossRef](#)] [[PubMed](#)]
35. Allen, P.B.; Dynes, R.C. Transition temperature of strong-coupled superconductors reanalyzed. *Phys. Rev. B* **1975**, *12*, 905–922. [[CrossRef](#)]
36. Manjon, F.J.; Tiginianu, I.; Ursaki, V. *Pressure-Induced Phase Transitions in AB₂X₄ Chalcogenide Compounds*; Springer: Berlin, Germany, 2014. [[CrossRef](#)]
37. Dresselhaus, M.; Dresselhaus, G.; Jorio, A. *Group Theory—Application to the Physics of Condensed Matter*; Springer: Berlin, Germany, 2008. [[CrossRef](#)]
38. Lv, B.Q.; Feng, Z.L.; Zhao, J.Z.; Yuan, N.F.Q.; Zong, A.; Luo, K.F.; Yu, R.; Huang, Y.B.; Strocov, V.N.; Chikina, A.; et al. Observation of multiple types of topological fermions in PdBiSe. *Phys. Rev. B* **2019**, *99*, 241104. [[CrossRef](#)]
39. Mardanya, S.; Singh, B.; Huang, S.M.; Chang, T.R.; Su, C.; Lin, H.; Agarwal, A.; Bansil, A. Prediction of threefold fermions in a nearly ideal Dirac semimetal BaAgAs. *Phys. Rev. Mater.* **2019**, *3*, 071201. [[CrossRef](#)]